Relating convergence of the actuator line method to its velocity sample using a novel description of the bound vortex in time-dependent fluid dynamics simulations

Evert Ivo Wiegant[1], Delphine de Tavernier[1], and Axelle Viré[1]

[1]Delft University of Technology

Correspondence: Evert Ivo Wiegant (e.i.wiegant@tudelft.nl)

Abstract. The actuator line method (ALM) is a popular method for representing wind turbine blades in computational fluid simulations. It utilizes a model to compute aerodynamic forces that requires an undisturbed flow velocity relative to the blade. However, the input velocity and output forces are sampled and applied locally; within the bound vortex that forms around the blade, and is thus disturbed. This inherent conflict translates to a strong dependency of the outcome of the simulation, and its convergence, on the sampling approach. This work presents a quantitative description of the bound vortex, and thereby the disturbance on the sampled velocity, in time dependent simulations (e.g. large eddy simulations, LES). The properties of the bound vortex were found to be a function of the single parameter $\Lambda = \Delta s / \epsilon$; the relative distance travelled by an ALM node within one time step, divided by the ALM kernel size. We use simulation data to validate this description and demonstrate that convergence of simulations can largely be attributed to the disturbance from sampling within the bound vortex. Consequently, this attribution to an erroneous process implies that convergence of the ALM is only partly related to the degree of representation of the relevant physical phenomena, which convergence is often assumed to imply. We propose that one must either ensure the disturbance is adequately accounted for, or that an alternative convergence criterion is to be used. We further use the description of the bound vortex to explain that a certain class of velocity sampling methods can indeed successfully account for the disturbance; removing the error and bringing simulations closer to convergence, yet that a correction based on the present description of the bound vortex would be more computationally efficient.

1 Introduction

The actuator line method (ALM) has been a popular choice for simulating wind turbines in computational fluid dynamics (CFD) simulations since its description by Sørensen and Shen (2002). In such simulations blade forces are modelled, allowing for a flow solution that includes the blades without needing the detail to fully resolve flow around their intricate geometry. Its use is motivated by contemporary society's need to decarbonize its energy systems, which motivates development of technologies to harvest energy sources that renew on small time scales. One such technology, the wind turbine, is increasingly designed to be used in harsher and more remote environments (Soares-Ramos et al., 2020). Numerical methods, among which the ALM, are much relied upon to study how these turbines fare in a variety of flows (Amiri et al., 2024), of which some recent examples

include flows related to; motions of floating wind turbines (Li et al., 2025), active wake control (Gutknecht et al., 2025), and complex terrain (Mi et al., 2025), to name a few.

Despite its wide and frequent use, there is no thorough consensus on how the ALM is best operated, nor is it well understood how it affects the outcome of a simulation. In this work we aim to address the topics of convergence of simulations and velocity sampling using a quantitative description of the bound vortex, and discuss best practices regarding computational efficiency and accuracy. We first introduce how the ALM operates and how it is treated in literature before further introducing its problems.

1.1 Operation of the ALM

The ALM represents blades of a wind turbine by lines of nodes, where each node is associated with a section of the blade. The ALM operates in 3 steps per timestep or iteration; sampling the velocity vector from the CFD field, computing the aerodynamic forces, and projecting these forces onto the CFD grid. Each of these steps is the subject of active research.

The first step, sampling the local flow velocity, involves some form of interpolation of the CFD field on one or multiple points near each node. The original description of the ALM by Sørensen and Shen (2002) uses a velocity that is sampled at the location of the node; a single point. Some variations on this single point sample use different interpolation methods (Jha et al., 2014; Mittal et al., 2015) or a shifted location with respect to the force projection (Martínez-Tossas et al., 2017). While the original single point approach is still widely used, there is apparent preference for sampling methods that utilize multiple points. Many such methods are proposed in literature, such as sampling within a volume around the node (Churchfield et al., 2017), or along various shapes of lines in proximity to the node (Jost et al., 2018; Sanvito et al., 2024; Muscari et al., 2024). The principles behind these velocity sampling methods are generally based on the assumption of symmetry, or other principles that are strictly only valid for the steady state situation (Churchfield et al., 2017; Martínez-Tossas et al., 2017; Jost et al., 2018). However, these methods are applied (without adjustment) to time-dependent simulations as well (Churchfield et al., 2017; Zormpa et al., 2025).

The second step, computing the aerodynamic forces, uses the sampled velocity and a look-up table of aerodynamic coefficients associated with the airfoil at each node. These look-up tables (polars) are constructed in controlled environments (e.g. wind tunnel or CFD simulation) and relate undisturbed flow to lift and drag on the airfoil. The main assumption of the ALM is thus that local 3D effects at the blades can be described using polars that map from an undisturbed velocity to the force vector on a 2D airfoil. Various corrections can be found in literature to make these 2D polars more applicable to the 3D situation, most commonly addressing tip behaviour (Martinez-Tossas and Meneveau, 2019; Taschner et al., 2023; Forsting et al., 2019; Kleine et al., 2023). Additionally, the validity of applying 2D polars to the 3D situation and the role of the force projection (discussed next) was studied by Melani et al. (2024).

The third step, applying (or "projecting") the aerodynamic forces to the fluid, is done by smearing the force from each node to the CFD cells around it. In reality, a blade section accelerates fluid as it passes over a (2D) surface, while a CFD model uses a 3D grid. This requires a choice to be made about what volume of fluid the blade section is to accelerate. The force is distributed on grid cells around the node using a Gaussian kernel, where choices include the shape (Jha et al., 2014; Martínez-Tossas et al., 2017; Churchfield et al., 2017; Melani et al., 2024) and central coordinate of the kernel (Martínez-Tossas et al., 2017), as well as

its size. An optimal kernel size, usually denoted by ϵ, was expressed in terms of the chord length of the local airfoil and grid cell size by Shives and Crawford (2013). Since their recommendation is quite computationally demanding, the earlier suggestion

60 by Troldborg et al. (2010) of $\epsilon = 2\Delta x$ (where Δx is the grid cell size) is still commonplace. However, this result is based on arguments of numerical stability, rather than accuracy or convergence. Most common is the spherically symmetric Gaussian shape, about which Melani et al. (2024) have concluded that it allows for better subsequent velocity sampling. Although there is general consensus on a size of $\epsilon \geq 2\Delta x$, its exact value varies from problem to problem.

1.2 Consensus on velocity sampling and the bound vortex

65 A problem inherent to this three-step operation is that the force projection of step 3 disturbs the velocity sample of step 1 of the next iteration or time step. This is in conflict with the aerodynamic routine of step 2, which requires an undisturbed velocity. This interaction between projection and sample is addressed to some extent in most, if not all, ALM studies, though most directly in work on velocity sampling. Many studies propose averaging multiple samples of flow velocity in a region around the node using some specific configuration, yielding better results in terms of cancelling the disturbance and increasing

70 robustness (i.e. less dependent on numerical parameters) of power and rotor thrust compared to using the sample at a single point. Some examples of configurations are; a volume the shape of the kernel (Churchfield et al., 2017), a circular line around the node (Jost et al., 2018), a pair of straight lines before and behind the rotor (Sanvito et al., 2024), and a line ahead of the airfoil (Muscari et al., 2024), to name a few. The motivation behind these configurations of multiple samples is to account for the bound circulation one way or another, yet their number is testament to the lack of consensus.

75 At the same time, the analytical study of Martínez-Tossas et al. (2017) advocates for sampling at a single point. They describe the flow field near the actuator line (AL) as a superposition of analytical steady state solutions of the flow subject to the lift and drag forces separately. They show that the lift-only solutions results in a vortex around the blade. They then proceed to use their result to find the optimal sampling location, which, for the lift-only case, is simply at the centre of the vortex where the induced velocity is zero; at a single point. However, their assumption of steady state makes their solution invalid for time-dependent

80 simulations.

1.3 Convergence of simulations

Velocity sampling methods that utilize multiple points also seem to enhance robustness (i.e. decreased sensitivity to numerical inputs, which indicates proximity to the point of convergence) of the simulation. The works of Zormpa et al. (2025) as well as Muscari et al. (2024) have shown that the variation in loads and performance (i.e. rotor thrust and power) is reduced for some

85 velocity sampling methods with respect to others. The work of Liu et al. (2022) also exemplifies convergence with respect to numerical settings (grid and blade resolutions) outside the context of velocity sampling.

Practically, convergence is often associated with how well the relevant physical phenomena are represented, since adding more detail (thereby changing an input) to a simulation that already appropriately represents all relevant physical phenomena will not lead to a better representation (it was already appropriate). We argue that for simulations using the ALM, the flow

90 solution may have become insensitive to changes in numerical settings, indicating appropriate representation, while another

process (related to sampling a disturbed flow) may not. This would lead one to mistake the lack of convergence for inappropriate representation of the relevant physical phenomena, persuading the modeller to use more computational resource than necessary. We demonstrate that some velocity sampling methods found in literature are effective solutions to this problem, yet they still make inefficient use of computational resource by discarding detail. A correction based on the present description of the bound vortex is proposed as a solution to both problems.

1.4 Contributions of this work

In this work we address the problem of how past force projections at discrete time steps affect the future velocity sample. We present a quantitative description of velocities as they would be sampled within the bound vortex that results from these discrete projections (section 2.2). We describe our numerical set-up (section 2.3), then present two analyses; one to validate the present description of the bound vortex (section 3.1), another that demonstrates the extent to which the outcomes of the simulations (and convergence thereof) depend on the error made upon sampling in the bound vortex (section 3.2). We use the present description of the bound vortex to provide a detailed explanation of this variation in outcomes and the role of the velocity sampling used. Our discussion provides key insights on:

1. The consensus, or lack thereof, on velocity sampling methods (section 4.1).

2. The penalty in computational expense of the most prevalent type of velocity sampling methods, i.e. those that average multiple points (section 4.3).

3. The notion of representation of relevant physical phenomena and how it is related to convergence (section 4.2).

2 Methods

The method central to this work is the quantification of the bound vortex. We first present a general description of the ALM which provides context for the rest of this work. We then present the derivation of the bound vortex, followed by the description of the software and simulation set-up used to validate it.

2.1 Operation of the actuator line method

Central to the ALM is its computation of the aerodynamic force:

$$
\begin{bmatrix} L \\ D \end{bmatrix} = \frac{1}{2}\rho cl \begin{bmatrix} C_L(\alpha) \\ C_D(\alpha) \end{bmatrix} V_\infty^2
\tag{1}
$$

denoting the lift force, drag force, air density, chord length, blade section length, lift coefficient, drag coefficient, inflow angle of attack, and inflow velocity by L, D, ρ, c, l, C_L, C_D, α and V_∞ respectively. The lift and drag coefficients are determined from controlled environments, such as wind tunnel experiments or blade resolved simulations of the 2D airfoil, where the inflow velocity is representative for the free stream. This routine requires the velocity vector as input (V_∞ and α), which is

acquired in a preceding velocity sampling step, and outputs a force vector (L and D), which is projected in the subsequent
120 force projection step onto each nearby CFD grid point with a weighting function (per Sørensen and Shen (2002))

$$\eta(r) = \frac{1}{\epsilon^3 \pi^{3/2}} \exp[-(r/\epsilon)^2], \tag{2}$$

with r the distance between the ALM node and respective CFD grid cell and ϵ the kernel size. These three steps (velocity sampling, aerodynamic routine, force projection) are executed at each node at each time step before advancing to the next, such that the velocity is sampled a distance Δs away from its previous location relative to the flow, where the force projection
125 was centred. This distance may be approximated as $\Delta s \approx V_{rel} \Delta t$, with V_{rel} the velocity of the AL node relative to the actual flow (i.e. as it appears in the CFD field, thus including disturbances). We can only approximate this quantity, since the notion of moving relative to the flow is ambiguous in the Eulerian framework of the CFD solver.

2.2 Derivation of the disturbance velocity

We first isolate the quantity we aim to describe. We consider how the sampled velocity relates to the velocity that is actually
130 required by the aerodynamic routine; V_∞ of Eq. (1). This required velocity is defined in the airfoil frame as the "free stream" undistributed velocity. The velocity that would be sampled in this frame, $\boldsymbol{V}_{s,AF}$, contains an additional disturbance velocity, $\boldsymbol{V}_d$ due to local effects

$$\boldsymbol{V}_{s,AF} = \boldsymbol{V}_\infty + \boldsymbol{V}_d \tag{3}$$

which becomes

135 $$\boldsymbol{V}_s = \boldsymbol{V}_u + \boldsymbol{V}_d \tag{4}$$

when translated to the reference frame of the CFD. The subscripts s, u and d indicate the sampled, undisturbed and disturbance velocities respectively, subscript AF indicates the airfoil frame and $\boldsymbol{V}_\infty$ indicates the free-stream velocity (also in the airfoil frame) as required by the aerodynamic routine. We propose that this disturbance is due to the bound vortex, similar to the vortex found by Martínez-Tossas et al. (2017) which is valid for steady state. The effects of disturbances from other phenomena are
140 addressed when discussing the validation and simulation set-up (section 2.3) and in appendix A and are ignored for now.

We wish to describe the bound vortex, and thereby the disturbance, as it occurs in time-dependent simulations. By introducing the time dimension, we deviate from steady state in two ways:

1. We introduce a future: A future sampling location may move relative to the flow structure caused by the current force projections.

145 2. We introduce a past: The current flow structure is the result of having been forced at progressively shifting locations in the past.

We choose to describe the bound vortex using a type of Lamb-Oseen vortex with centre coordinate $\boldsymbol{x}_0$ and viscous core radius r_v. This assumption is justified by the recurring association of Lamb-Oseen vortices with the actuator line, regarding
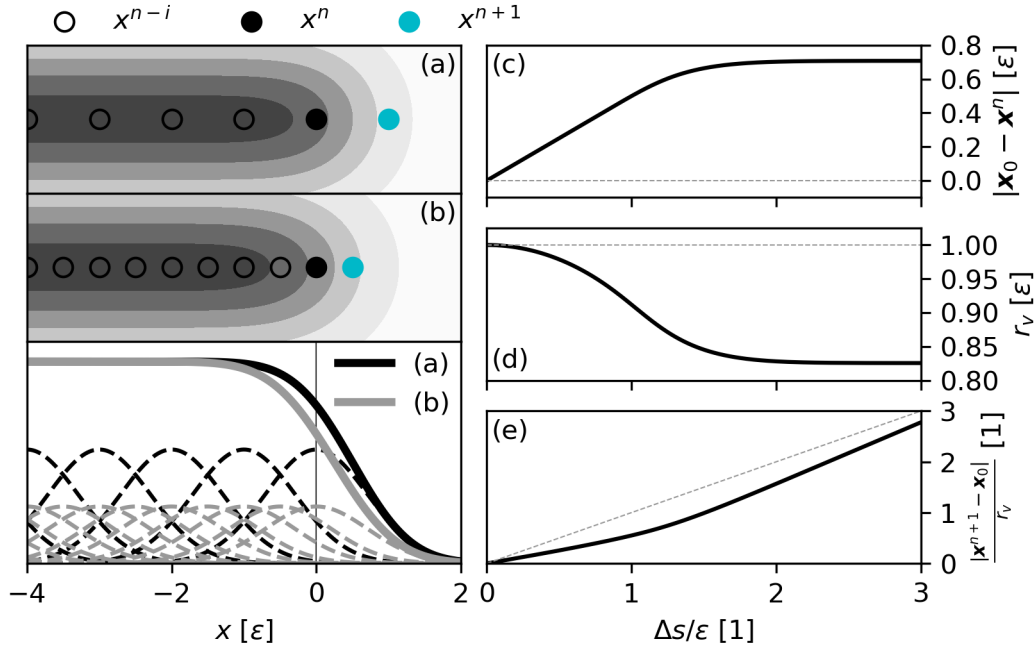
Figure 1. Left, panels (a) and (b): sketches of velocity fields due to discrete velocity increments with two different ratios of distance between locations of an AL node at subsequent time steps and kernel size; $\Delta s/\epsilon = \{1, 0.5\}$ for panels $\{(a), (b)\}$ respectively. Open, solid black, and solid blue dots show the previous, current, and next locations of the node respectively. The bottom left graph shows the associated single (dashed lines) and cumulative (thick lines) velocity increments. On the right, panels (c) and (d) show the derived vortex properties, following Eq. (10-12). Panel (e) combines both properties and assumes a sampling location at the future location of the node.

the bound vortex (Martínez-Tossas et al., 2017) as well as vortices in the wake (Dag, 2017; Forsting et al., 2019). By allowing

150   the vortex to be evaluated at any location $\boldsymbol{x}$ that is not necessarily the centre of the vortex, we adhere to deviation 1:

$$\boldsymbol{V}_d(r) = V_0 \frac{r_v}{|\boldsymbol{x} - \boldsymbol{x}_0|} \left(1 - e^{-|\boldsymbol{x} - \boldsymbol{x}_0|^2 / r_v^2} \right) \tag{5}$$

with

$$V_0 = \frac{\Gamma}{2\pi r_v} = \frac{L}{l \rho V_{rel} 2\pi r_v} \tag{6}$$

where $r = |\boldsymbol{x} - \boldsymbol{x}_0|$ is the distance of the sample from the vortex centre, L and Γ are the (current) lift and circulation respectively

155   of the AL, l is the length of the node's blade section and ρ is the air density. The velocity defined in Eq. (6), with which we scale velocities henceforth, is the velocity that is found at a distance r_v from the centre of a vortex, given that all lift force is applied somewhere within that radius. Note that the expression is given in polar coordinates, where $r = |\boldsymbol{x} - \boldsymbol{x}_0|$, and that the vortex properties ($\boldsymbol{x}_0$ and r_v) are yet unknown.

Next, we consider deviation 2, which states that subsequent forcing of previous time steps have gradually shifted positions.

160   Panels (a) and (b) of Fig. 1 show sketches of how such gradually shifting forcing affect velocities in 2D for two situations

that differ by their ratio of distance between subsequent node locations (Δs) and the kernel size (ϵ). Graphs of these velocities in 1D show that the situation of larger $\Delta s/\epsilon$, panel (a), is associated with stronger but fewer velocity increments (dashed black lines), while the smaller $\Delta s/\epsilon$, panel (b), is associated with weaker but more numerous velocity increments (dashed grey lines). The cumulative velocity increments of both situations (thick black and grey lines) become equal some distance to the left or right of the node's current position (at $x = 0$). We thus see uniformly accelerated flow on either side of the AL with a transition region in between where the velocity gradient is non-zero, which in the case of the lift-only situation, is in a cross-flow direction. Following the definition of vorticity, a vortex (i.e. a region of local maximum vorticity) is associated with a cross-flow gradient. We can therefore deduce the vortex properties of the flow induced by the AL by considering this graph of cumulative velocity increments. The cumulative velocity increment at any location x and time step n is as follows;

$$\Delta \mathcal{V}(x) = \sum_{n}^{N} \Delta V_n \eta(x - x_n) \tag{7}$$

with the velocity increment from the node at time step n

$$\Delta V_n = \int_{t^{n-1}}^{t^n} a_{n-1} dt \tag{8}$$

whose exact value depends on the integration scheme used, with x_n the location of the node at that time step and N indicating the current time step. While the velocities of Eq. (8) and (7) are used to compare situations in which the magnitude of velocity increments differ (e.g. simulations with different time steps or kernel sizes, as is shown in Fig. 1), the vortex properties in any particular set-up may also be derived from the dimensionless cumulative kernel:

$$H(x) = \sum_{n}^{N} \eta(x - x_n) \tag{9}$$

By doing so, the result will be generally applicable to any simulation, independent of its set-up or specific flow field during runtime. However, we have implicitly assumed that lift is constant in time, which becomes questionable when variations in lift occur much faster than the time it takes for the node to move away from contributions of previous force projections, i.e. the distance of a few ϵ.

We define the vortex centre x_0 as the inflection point of H and the vortex radius r_v as the distance between the inflection point and the point where the cumulative kernel reduces to $1 + \mathrm{erf}(-1)$ of the value at the inflection point, i.e. the value of a Gaussian cumulative distribution function at ϵ from its inflection point:

$$H''(x_0) = 0 \tag{10}$$

$$H(x_r) = H(x_0)[1 + \mathrm{erf}(-1)] \tag{11}$$

$$r_v = |x_r - x_0| \tag{12}$$

Equations (10) and (11) are solved numerically for x_0 and x_r. The resulting vortex properties turn out to be a function of the single parameter that is the ratio of distance between subsequent node locations and the size of the AL kernel, $\Delta s/\epsilon$, as shown
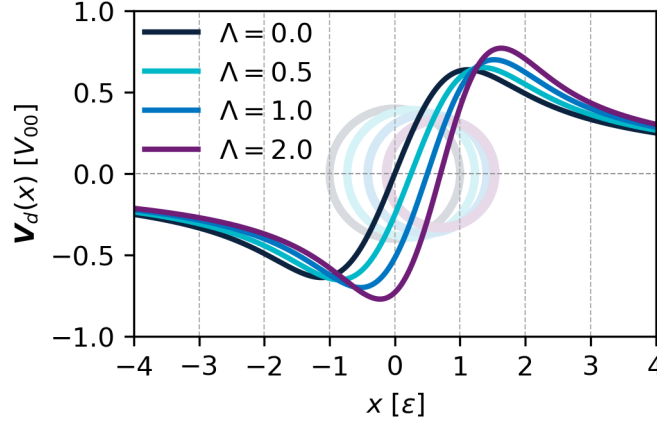
Figure 2. The disturbance velocity (bound vortex) per Eq. (5) in Cartesian coordinates, shown with vortex centre locations and radii for different Λ. The faded circles share centres and radii of the respective vortices and are solely for illustration. The y-axis is scaled with the characteristic velocity (Eq. (6)) at $\Lambda = 0$, i.e. $V_{00} = V_0|_{\Lambda=0}$.

190   in the panels (c) and (d) of Fig. 1. To stress its use as a parameter rather than a measure of space (i.e. distance between nodes), we use the symbol $\Lambda = \Delta s/\epsilon$ when we refer to it in that role. This parameter is mostly determined by numerical settings and can be estimated prior to the velocity sampling step using the aforementioned $\Delta s \approx V_{rel}\Delta t$ (section 2.1). Interestingly, the vortex properties reach their steady state equivalents at $\Lambda = 0$ (dashed lines in the right panels of Fig. 1, following Martínez-Tossas et al. (2017)), thus when individual velocity increments are infinitely closely spaced and infinitesimally small. Note that

195   although the vortex properties can be plotted (right panels of Fig. 1), we do not know their exact expressions. In our analyses to come, they are retrieved using high order polynomial fits of the shown graphs.

We have completed our description of the bound vortex valid for the time-dependent situation. It is the assumed Lamb-Oseen vortex whose properties can be derived from the cumulative ALM kernel. It is found to solely depend on the parameter Λ. As Λ increases (i.e. increasing Δt or decreasing ϵ) the bound vortex shifts forward in the direction of the node's motion relative to

200   the flow, and it shrinks. This is illustrated in Fig. 2.

2.3   Validation and model set-up

We aim to validate our description of the disturbance velocity of Eq. (5) using simulation data. Since the disturbance velocity cannot simply be got from simulation data, we estimate it using Eq. (4), which we combine with Eq. (5) to get:

$$\frac{|\boldsymbol{V}_s - \boldsymbol{V}_u|}{V_0} = \frac{r_v}{|\boldsymbol{x} - \boldsymbol{x}_0|}\left(1 - e^{-|\boldsymbol{x}-\boldsymbol{x}_0|^2/r_v^2}\right) \tag{13}$$

205   $\boldsymbol{V}_d$ (Eq. (5)) is expressed in polar coordinates, thus we evaluate $\boldsymbol{V}_s - \boldsymbol{V}_u$ in polar coordinates as well. We simplify the procedure by only validating the absolute value of the disturbance velocity, indicated by the absolute value operator on the

left-hand side of Eq. (13). We have also moved V_0 to the left-hand side of the plot, removing some of the scale difference between simulations such that their results may be shown in a single plot.

The velocity sample $\boldsymbol{V}_s$ that we use for validation is taken at the location of where the future force projection will be. By doing so, the right-hand side of Eq. (13) requires only the mapping of the bottom right graph of Fig. 1 from the estimated $\Lambda = V_{rel}\Delta t/\epsilon$. The left-hand side contains a number of velocities that we acquire from the CFD: $\boldsymbol{V}_s$ is the velocity as it is sampled, including disturbances, V_0 is computed from the force as it was last applied to the CFD, which we get by assuming $L \approx F$ in Eq. (6), thereby neglecting drag, and lastly, $\boldsymbol{V}_u$, the undisturbed velocity as the aerodynamic routine requires it. There is no straightforward way to acquire $\boldsymbol{V}_u$ from simulation data, yet there are situations in which its value may be reasonably assumed. Our numerical set-up is therefore mainly constrained by being able to estimate $\boldsymbol{V}_u$, while it is driven by our desire to validate Eq. (5) as generically as possible.

We estimate $\boldsymbol{V}_u$ at every time step and every node of each blade as the annular average velocity at that time and in the annulus of the radius of that node:

$$\boldsymbol{V}_u(t,r) \approx \int\limits_0^{2\pi} \boldsymbol{V}(t,r,\phi)\,d\phi = \langle \boldsymbol{V}(t,r)\rangle_{\mathrm{ann}} \tag{14}$$

In a simulation of a flat rotor (stiff straight blades with no cone angle nor rotor tilt) and uniform inflow, there are two arguments by which this assumption is valid:

- BEMT: In such a set-up, blade element momentum theory (BEMT) is reasonably valid. BEMT, through its use of momentum theory, uses a single velocity to describe flow through an annulus, which, following conservation of mass, equates the average in the annulus.

- Symmetry: The vortex (with viscous core) is an antisymmetric phenomenon, where the undisturbed flow is found in its centre (Eq. (5) approaches 0 as $\boldsymbol{x}$ approaches $\boldsymbol{x}_0$). Averaging the velocity symmetrically along the extent of the phenomenon therefore gives a robust estimate of the undisturbed velocity. This is confirmed after performing the simulation for the axial component (black line of Fig. 4).

We thus consider this quantity to adequately represent incoming flow to the AL's airfoils that is unaffected by the airfoil itself. In fact, it mostly accounts for induction of the turbine, which strongly affects the flow but is a non-local effect and thus rightfully accounted for by $\boldsymbol{V}_u$. The role of other local effects (e.g. the tip vortex) is discussed in appendix A.

Our validation is done for a variety of conditions within the aforementioned constraints. We vary those parameters that directly affect our description (i.e. time step, kernel size and wind speed), as well as the spatial resolution (Δx). Values of these parameters are shown in Table 1. In addition to the settings mentioned in Table 1, all simulations use a uniform cubic grid, a concurrent precursor set-up with periodic boundary conditions (Stevens et al., 2014), a sub-filter model as described by Rozema et al. (2015) with a model constant $C = 1/3$, a domain size of at least $6.4D \times 4.26D \times 4.26D$, and are run for 450 seconds, of which the last 220 are used for analyses. As it takes roughly 220 seconds for flow in the simulation with the lowest wind speed (6.98m/s) to have traversed the domain, this ensures that each simulation has spun up with at least one traversal

Parameter	Values	Unit
Δx	4, 6, 8	m
U_∞	6.98, 8.785, 10.59	m s^{-1}
ω	5, 6.275, 7.55	RPM
Δt	0.25, 0.5, 1.0, 1.5	$\frac{\Delta x}{\omega R}$
ϵ	1, 1.5, 2, 3, 4	Δx

Table 1. Simulation inputs used for verification of Eq. (13). Wind speed and rotor speed (U_∞ and ω) are varied together, indicated by their shared box. This results in $3 \cdot 3 \cdot 4 \cdot 5 = 180$ different simulations.

of the flow (through its periodic boundaries) and that the analyses use the flow of the entire domain. Although we expect the

240 present description of the bound vortex to be valid independent of runtime, this may not be the case for the quantities we use to validate it. The undisturbed velocity $\boldsymbol{V}_u$ involves averaging velocities across the rotor. Since flow across the rotor does not uniformly respond to changes at the blade, the value of $\boldsymbol{V}_u$ will contain history of the flow. Only when this flow history is equal to the present flow will $\boldsymbol{V}_u$ be an accurate representation of the undisturbed flow as required by the aerodynamic routine. We must therefore validate using simulations that have reached a steady state.

245 **2.4 Software**

We simulate a modified ("flat" rotor) variant of the IEA 15MW reference wind turbine model using a coupling between the LES framework ASPIRE and the wind turbine simulator OpenFAST. This coupling has previously been used by Taschner et al. (2023).

ASPIRE utilizes the GPU-Resident Atmospheric Simulation Platform (GRASP), which is a LES solver that shares ancestry

250 with the Dutch Atmospheric Large Eddy Simulation (DALES, Heus et al. (2010)) and has seen separate development since being ported to the GPU (Schalkwijk et al., 2012). ASPIRE provides users access to the main (time) loop of the simulation, allowing it to interface with other codes such as OpenFAST.

OpenFAST is a open-source code developed by NREL (Jonkman et al., 2024) and is used to simulate one or multiple aspect of a wind turbine, such as the aerodynamics of the rotor, elastic response of the structure, actuation of its servo, etc., by enabling

255 or disabling its various modules.

The coupling between ASPIRE and OpenFAST is established through ASPFAST (Folkersma, 2023), which is called by the main loop of ASPIRE and makes subsequent calls to the OpenFAST API. It also contains the velocity sampling and force projection routines of the ALM, while aerodynamics are handled by OpenFAST using its blade-element theory (BET) routine. The velocity sampling involves linearly interpolating to the node location from the 8 (in 3D) surrounding points. The force of

260 a node is projected onto the CFD grid as described following the original implementation (Sørensen and Shen, 2002) by taking the convolution of the force with the regularization kernel of Eq. (2).
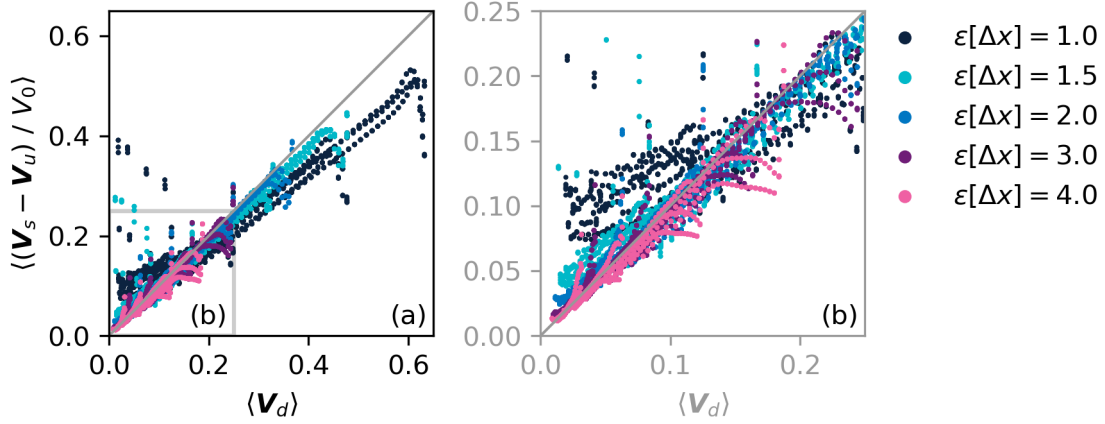
Figure 3. Scatter plots of time-averaged simulation data, comparing the left-hand side estimation of the disturbance velocity (Eq. (13), y-axis) with its right-hand side description (x-axis), including a variety of simulation settings and input conditions (see Table 1). Panel (b) is a zoomed in version of panel (a). Different colours were used to dissect the data in a way that the authors deemed appropriate; by grouping simulations of equivalent kernel sizes, and holds no significance otherwise.

3 Results

In the following section we present two types of analyses. We first validate the description of the bound vortex, thereby concluding the description itself. Second, we present an analysis to explore how sampling within the bound vortex relates to

265 convergence, which forms the basis for further discussions.

3.1 Validation of the absolute disturbance velocity

We create a scatter plot with the left-hand side of Eq. (13) on the y-axis and its right-hand side on the x-axis. For each AL node in each simulation at each time step, both sides of Eq. (13) are computed before being averaged in time, yielding a point for each node in each simulation. The resulting scatter plot will show whether our model of the disturbance velocity (rhs) matches

270 its estimate from simulation data (lhs), by the degree at which it follows the $y = x$ line. We present the scatter plot in Fig. 3. We excluded data from nodes that are closer than 2ϵ from the centre of the rotor to avoid overlap between kernels of different blades.

We observe that most points lie close to the $y = x$ line, thereby confirming that flow near AL nodes generally behaves as described by Eq. (13) and by extension, Eq. (5). We further see that groups of points originating from the same simulation tend

275 to arrange themselves forming trajectories related to their relative positions on the blade. Points near the root/tip of the blade are associated with low/high Λ, which is the result of low/high relative velocity, which results in smaller/larger disturbances (as long as the disturbance is monotonic with respect to Λ, which is the case for our simulations). The scale of this trajectory depends on the chosen Δt and ϵ of the simulation, such that the largest values on the x-axis are populated by nodes near the
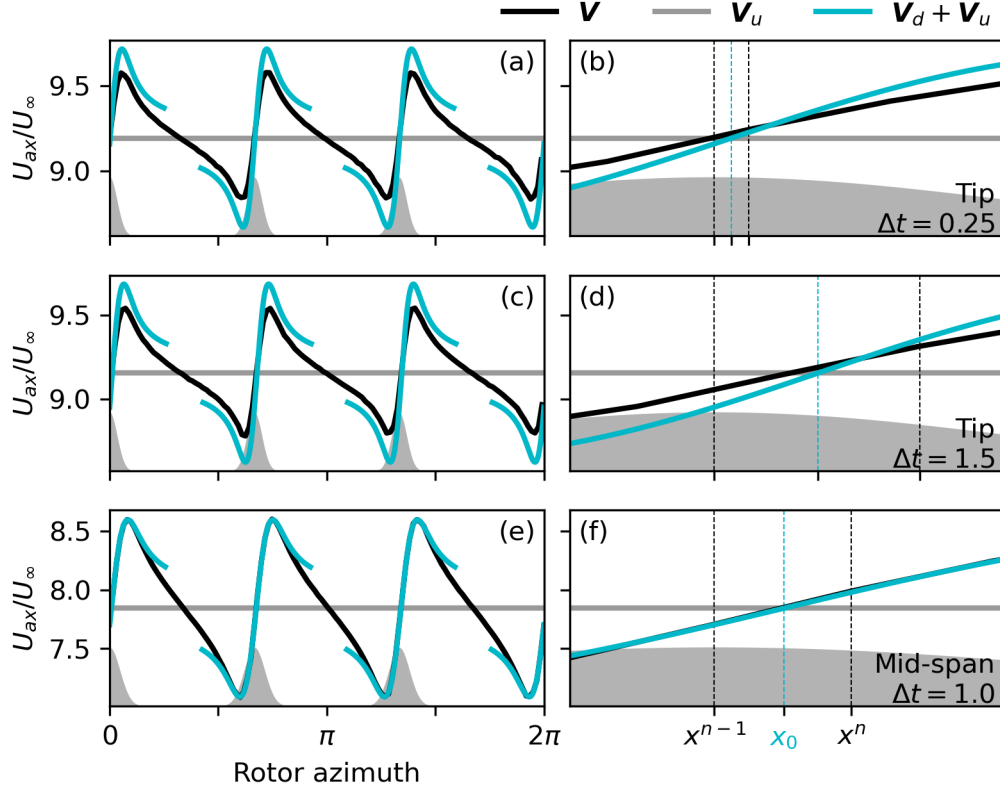
Figure 4. Velocities along an annulus of the rotor V, their average V_u per Eq. (14), and the present description of the bound vortex $V_d + V_u$ per Eq. (5). The annulus is located across the tips of the blades in panels (a), (b), (c) and (d) and closer to mid-span (at $r/R = 0.7$) in panels (e) and (f), showing velocities of simulations that only differ in time step size ($\Delta t = 0.25 \frac{\Delta x}{\omega R}$ for panels (a) and (b), $\Delta t = 1.5 \frac{\Delta x}{\omega R}$ for panels (c) and (d), $\Delta t = 1.0 \frac{\Delta x}{\omega R}$ for panels (e) and (f)). The right panels show the same data as their respective left panels, but zoom in on a single blade, with indicated on the x-axis the positions of the last force projection x^n, which is also the centre of the Gaussian shape, the next velocity sample x^{n+1}, and the vortex centre x_0 as presently described. The figure demonstrates situations in which points of the scatter plot of Fig. 3 deviate upwards (panel (b), where $V > V_d + V_u$ at x^{n+1}), and downwards (panel (d), where $V < V_d + V_u$ at x^{n+1}), which we relate to a combination of the finite cylinder effect and induction of the tip vortex, as well as demonstrate where points lie close to the $y = x$ line of Fig. 3 (panel (f) of the present figure, where $V \approx V_d + V_u$ at x^{n+1}) where those effects are absent.

tips of the blades in simulations of the smallest kernel size and largest time step (e.g. points above $x > 0.5$ originate from
280   simulations with $\epsilon = 1.0\Delta x$ and $\Delta t = 1.5 \frac{\Delta x}{\omega R}$) and include all spatial resolutions and inflow wind speeds. Some deviations from the $y = x$ line can also be seen, most notably the downwards (in the y-direction) deviation for larger values on the x-axis and the upwards deviation visible for some pink and purple trajectories ($\epsilon = 3\Delta x$ and $\epsilon = 4\Delta x$ respectively) below $x < 0.1$. These deviations can largely be attributed to the induced velocity by the tip vortex and the finite cylinder effect, both of which we shall shortly discuss.

285   The induced velocity of the tip unevenly affects the sample and the annular average velocity, i.e. $\boldsymbol{V}_s$ and the estimate of $\boldsymbol{V}_u$. As the tip vortex trails behind the blade, a large portion of the annulus is affected by it. At the same time, since the sample occurs at the front of the blade, it is less affected it. Although the extent of this effect depends on time step, kernel size, and location on the blade, it generally causes a positive offset in $\boldsymbol{V}_s - \boldsymbol{V}_u$, thus on the y-axis. This effect is demonstrated in Fig. 4, where at x_0 the black line is above the blue line in panels (b) and (d).

290   The finite cylinder effect refers to the asymmetric kernel density near both ends of the blade (root and tip). Since most of the root region is excluded, we here discuss its effect on the tip region. As the force of each node is smeared in all directions, the node at the tip receives force contributions from neighbouring nodes only from one side. The bound vortex around the tip node is thus weaker than it is around a node at mid-span (which receives contributions from both sides) as the total lift smeared from all nodes is reduced. This weaker vortex is clearly visible in panels (a) and (c) of Fig. 4, with the peaks of the vortices in blue
295   overestimating the observed peaks in black. Panel (e) of the same figure shows this overestimation does not occur away from the tip. In terms of Eq. (5), this is indicated by a lower L (lift force), resulting in lower slopes within the vortex. This effect is more prevalent for large ϵ, for which more nodes are considered near the tip.

We thus have two ways in which the observed disturbance deviates from the presently described disturbance of Eq. (5); one causes an offset (the induced velocity of the tip), the other changes the slope within the vortex core (the finite cylinder).
300   Whether their combined effect results in a positive or negative deviation depends on where the velocity is evaluated, which is demonstrated in panels (b) and (d) of Fig. 4 by considering the values of the black and blue lines at x^n. The location of the sample x^{n+1} relative to the bound vortex depends on Λ (note that panels (b) and (d) show identical simulations except for their time step size and thus their value of Λ) and the specific velocity sampling method used.

Lastly, it is observed that simulations using the smallest kernel sizes ($\epsilon = \Delta x$, and $\epsilon = 1.5\Delta x$ to a lesser extent) deviate
305   downwards for larger values on the x-axis. We consider that the description of the bound vortex assumes the size of the viscous vortex core to be determined only by the size/shape of the cumulative kernel. As the flow is solved in time, the vortex strength is altered by a variety of processes such as subgrid eddy viscosity, numerical diffusion, or interpolation from the CFD field (upon sampling the velocity). These processes lead to a larger vortex core and/or smaller sampled velocities, all of which are more active/effective in presence of large gradients, thus for small ϵ. Note that values of $\epsilon < 2\Delta x$ are not at all commonplace,
310   they are included here regardless to evaluate the extend to which our present description of the bound vortex is valid.

3.2   Convergence

With the following analysis we study how sampling within the bound vortex affects convergence of simulations.

We present a type of analysis that is commonly found in literature, where the thrust or power coefficients are plotted for varying numerical inputs in order to estimate how well their simulations are converged. Examples can be found in the works of
315   Zormpa et al. (2025), Muscari et al. (2024) and Liu et al. (2022). Figure 5 shows the thrust coefficient C_t of the wind turbine for various time steps (Δt) and kernel sizes (ϵ). We show thrust coefficients of the entire rotor, panel (a), as is commonly found in literature, as well as the thrust coefficient of a single node, panel (b), which, since it associated with a single velocity and thus a single Λ, is expected to be more directly related to the disturbance from the bound vortex. Considering the faded colours
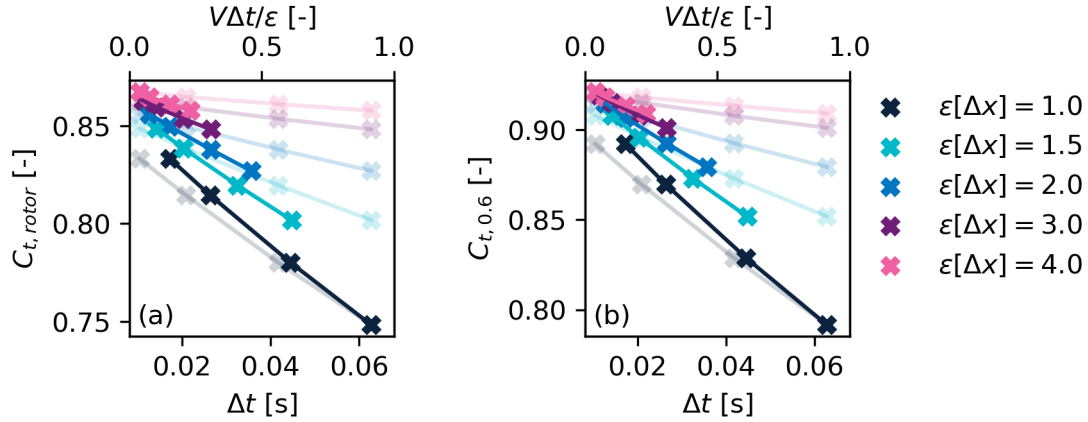
Figure 5. Thrust coefficients of a set of simulations of varying Δt and ϵ, with $\Delta x = 4$m and $U_\infty = 10.59$ms^{-1}. The coefficients are valid for the entire rotor, panel (a) and for the annulus at $r/R = 0.6$, panel (b), and are plotted against Δt in faded colours (bottom axis) and $V\Delta t/\epsilon$ in full colours (top axes). The velocity used to quantify the top axis ($V\Delta t/\epsilon$) is the relative velocity at $r/R = 0.6$.

first, we see that when using small time steps or large kernel sizes we are relatively close to convergence; at small Δt the effect
320 of ϵ on C_t is reduced and likewise, at large ϵ variations in Δt do not affect the outcome much. We recognize that small values of Δt and large values of ϵ both lead to small values of Λ. Additionally, we know of a mechanism that is quantified by Λ (i.e. sampling velocity within the bound vortex) which we also expect to affect C_t. We may therefore study to what extent variation in rotor thrust (or, C_t) is explained by this mechanism by studying to what extent it is explained by Λ. The validity of this statement (whether explanation by Λ implies explanation by the mechanism) is discussed in appendix B.

325 Now considering the full colours, Fig. 5 shows thrust coefficient for different values of Λ ($= V\Delta t/\epsilon$, top x-axes). We see that Λ is indeed better suited to explain variation in C_t than either of its constituent parameters. This implies that part of the variation in thrust can be attributed to the bound vortex. The explanation of variation is most evident for the thrust coefficient of a single annulus (panel (b) of Fig. 5), which, as mentioned, is more directly related to the disturbance from the bound vortex. We further address implications of this result in the discussion, section 4.2.

330 **4 Discussion**

Next we discuss implications and limitations of the present description of the bound vortex. The discussion on velocity sampling is motivated by explaining the behaviour of Fig. 3, which consequently provides insight into the success or detriment of the many velocity sampling methods found in literature. The discussions on convergence and representation of physical phenomena, and on applicability as a correction, consider new best practices based on insights of the description of the bound
335 vortex.
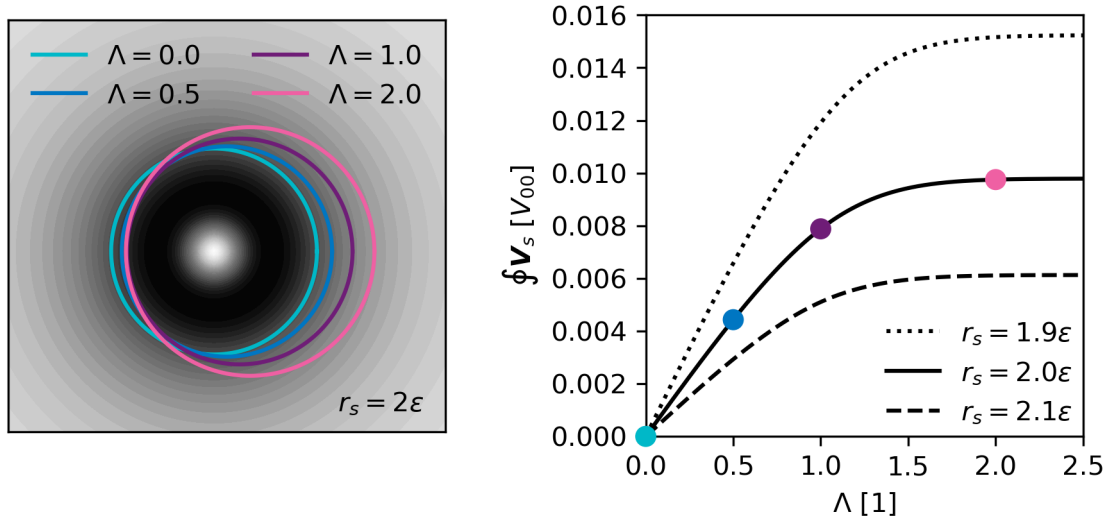
Figure 6. Demonstration of velocity sampling near the bound vortex (grey contours, left panel). The demonstrated method acquires the average velocity along a circle of radius 2ϵ, similar to the method of Jost et al. (2018). As Λ changes value, the vortex shifts and shrinks, which is visualized as the averaging circle shifting and growing instead, indicated for four values of Λ using coloured lines. The right panel shows how this circle-averaged velocity of the shifted and shrunk vortex varies with Λ, which determines the vortex properties. Dashed and dotted lines indicate the averaged velocity if a circle of a slightly different radius is chosen.

4.1 Velocity sampling

Many of the velocity sampling methods found in literature use the average of samples taken at multiple points using various possible configurations. These methods (using multiple points) are found successful and robust; they remove most of the disturbance and reduce dependency on input. Yet, there is no clear consensus on a single best sampling method.

340   The present description provides insight into why such methods may or may not work. Methods aiming to cancel the error, based on the principle of symmetry, are often centred on their respective AL node, which is not where the bound vortex may be located (Fig. 1, panel (c)) and thus their principle does not hold. However, we shall demonstrate that as long as the sampling occurs reasonably far away and exhibits sufficient symmetry, their resulting sampling errors will be low. Our demonstration, shown in Fig. 6 uses velocities that are sampled in a circle of radius 2ϵ around the node. This sampling method is similar to the

345   "LineAve" method introduced by Jost et al. (2018), which has seen recurring use (Melani et al., 2024; Zormpa et al., 2025). Our sampled velocity is computed by evaluating the bound vortex as described in the present work (Eq. (5)). The left panel of Fig. 6 shows a vortex (black/grey contours) and the circle along which "samples" are taken and averaged (light blue). As Λ increases, the vortex shifts and shrinks, which is equivalent to the sampling region shifting and growing, as indicated by coloured circles in the figure. The averaged velocity along the circle is shown in the right panel, with Λ values of the circles in

350   the left panel indicated on the graph. For increasing Λ, the sample contains an increasing error, plateauing for the largest values

shown where the vortex does not shift/shrink any more (apparent from Fig. 1, right panels). This error is of limited magnitude due to the symmetry and relatively large radius of the sampling configuration, leading to samples on one side of the vortex roughly cancelling those on the other. In fact, the demonstrated sampling method only yields a fraction of the error of a single point sampled within this shifting and shrinking vortex; at radius $r_s = 0$ (which corresponds to sampling at a single point) the

355   curve plateaus around $\oint V_s = 0.73V_{00}$ towards larger Λ, which is about two orders of magnitude larger than what is seen in the figure.

We may also understand why such a velocity sampling method is robust and thus why the works of Muscari et al. (2024) and Zormpa et al. (2025) show reduced sensitivity to numerical inputs by the simple act of changing how the velocity is sampled. As we have seen in Fig. 5, variation in the disturbance velocity explains part of the variation in rotor thrust between

360   simulations of different settings. Thus, if we can somehow reduce variation in the disturbance velocity, we would reduce variation in C_t, bringing the simulation closer to convergence. The right panel of Fig. 6 indeed shows greatly reduced variation between simulations (where simulations are differentiated by Λ, thus moving along the x-axis) compared to what would result from sampling at a single point. The strong dependency on the radius of the sampling method (comparing the different lines of Fig. 6, right panel), with the error becoming increasingly negligible for larger radii regardless of the exact properties of the

365   bound vortex (i.e. regardless of Λ), explains the success of some velocity sampling methods found in literature even while their assumptions (e.g. that of symmetry) were strictly incorrect.

As a rule of thumb, we conclude that when samples are taken sufficiently far from the node, using a configuration that is sufficiently symmetric around the node, the resulting velocity will have little disturbance and be robust. The veracity of this statement for any particular sampling method can simply be computed using Eq. (5).

370   ## 4.2   Convergence and representation of physical phenomena

Convergence, i.e. independence of the outcome of the simulation from its numerical inputs, is often considered to imply appropriate representation of physical phenomena that are relevant to the problem. We now argue for simulations using the ALM, that although one may approach convergence by using more costly numerical settings, it does not necessarily lead to better representation of the relevant physical phenomena. At some point, the relevant physical phenomena may be appropriately

375   represented while the numerical inputs still affect the outcome of an erroneous process. While the error may be reduced using more costly numerical settings, it may also be reduced some other way; by using a better velocity sampling method or a correction, thereby saving computational expense. For ease of argument, we assume an "explicit" operation of the AL, where the sampling and subsequent projection of a single time step both occur at the same location, before it steps to the next. For this case, the distance between sample and vortex is acquired from panel (e) of Fig. 1.

380   From Eq. (4) we see that on top of the desired velocity that is required by the aerodynamic routine (i.e. $\boldsymbol{V}_u$), there is an erroneous process (i.e. sampling within the bound vortex yielding $\boldsymbol{V}_d \neq 0$) affecting the outcome of the simulation. This erroneous process is affected by numerical settings in two ways (following Eq. (5)): (1) through the location and size of the vortex (x_0 and r_v), which change as a function of Λ and (2) through the location of the sample, $\boldsymbol{x}$, whose location relative to the previous force projection depends on the distance travelled since the last time step. While the former, (1), can be argued to

385 be related to the representation of physical phenomena (i.e. representation of the bound vortex), the latter, (2), has no physical (continuous) equivalent; it only exists because of the discrete time step. From Eq. (5) and Fig. 1, panels (c) and (d), we see that we can indeed avoid this error by changing our numerical settings; namely when we approach $\Lambda = 0$, at which $|x - x_0| \to 0$ and thus $\boldsymbol{V}_d \to 0$. However, approaching $\Lambda = 0$ requires infinite computational resources. Since the error caused by sampling in the bound vortex is predictable, described in this work, it is questionable whether we want to minimize $\boldsymbol{V}_d$ using numerical

390 settings alone. It would be more computationally efficient to minimize $\boldsymbol{V}_d$ some other way; through correction or an adequate velocity sampling method. Finding convergence of the solution then only concerns appropriate representation of the remainder, i.e. $\boldsymbol{V}_u$.

Proximity to convergence would then be more difficult to gauge, since $\boldsymbol{V}_u$ cannot easily be acquired from simulations directly. It requires the simulation to have properly accounted for $\boldsymbol{V}_d$ (thus, by the velocity sampling method or a correction),

395 such that convergence in the undisturbed velocity is reflected by convergence in turbine output, such as C_t. At the same time, in case $\boldsymbol{V}_d$ is not accounted for, Fig. 5 suggests a criterion may be formulated based on variation in output (e.g. C_t) for varying Λ. In principle, if all variation in output can be explained by variation in $\boldsymbol{V}_d$ (which in turn is solely described by Λ for disturbance by the bound vortex), the remainder explains no variation and is thus converged. More detail on the validity of this statement, as well as a more explicit continuation of the argument of representation of relevant physical phenomena, is found in appendix

400 B.

4.3 Applicability as a correction

While an average of multiple samples may be effective at reducing the disturbance velocity, so may a single sample with adequate correction. We next discuss an important, yet largely undervalued consequence of sampling at multiple points, then discuss the suitability of the present description (Eq. (5)) to be used as a correction.

405 A consequence of velocity sampling methods that sample and average at multiple points is that they reduce the effective resolution of the sampled velocity. By averaging multiple samples in a region, these methods effectively apply a spatial filter. The enhanced performance through spatial filtering (e.g. as found by Muscari et al. (2024) and Zormpa et al. (2025) and supported by the present work, Fig. 6) demonstrates that rotor-scale turbine behaviour is not dependent on the smallest scales (rotor-scale, since both works consider rotor thrust and power). This is the same principle of e.g. BEMT, which gives reasonably

410 accurate predictions of rotor loads and performance in situations of limited complexity by considering only rotor-scale flow phenomena (thus neglecting smaller scales). Therefore, by discarding detail, the respective ALM has effectively become a lower-fidelity method, yet at the same computational expense. At the same time, it is in those situations where increased complexity potentially leads to larger contributions of smaller scales (e.g. due to deflections of large blades (Chetan et al., 2022), or for floating offshore wind turbines interacting with their wake (Schulz et al., 2024)) where high fidelity methods such

415 as the ALM are particularly relied upon. Sampling at a single point on the other hand, does not cause such a reduction in detail (or much less, depending on the interpolation method used). If one could adequately correct for the disturbance velocity at a single point, it achieves exactly what a multiple-point velocity sampling method is intended to do (i.e. to omit $\boldsymbol{V}_d$ from the sample, following Eq. (4)), while retaining fidelity.

The present description of the expected error allows for correcting the disturbance during runtime, since its sole parameter Λ
is easily estimated. However, while the description (Eq. (5)) was found valid for time-averaged data (Fig. 3), velocity samples
and forces can vary substantially between time steps, even if the simulation has reached approximate steady state. These
variations in sampled velocity were most prevalent for smaller ϵ, which may correspond to the widely reported phenomenon
of oscillating loads for small ϵ (Troldborg et al., 2010; Shives and Crawford, 2013; Jha et al., 2014). Since this is not directly
related to the bound vortex or our description thereof, we recommend using the present description to correct for sampling
biases (i.e. average errors) caused by the bound vortex. This is done by subtracting the disturbance velocity of Eq. (5) from the
sample at each time step.

5 Conclusions

The bound vortex that forms at/near the actuator line causes the sampled velocity to contain an undesired disturbance. In this
work, we have formulated a quantitative description of the bound vortex as it occurs in time-discretized simulations (Eq. (5)).
The size and location of the bound vortex were found to be a function of the single parameter $\Lambda = \Delta s/\epsilon \approx V_{rel}\Delta t/\epsilon$; the
ratio of the distance between subsequent locations of a node and the kernel size, which is easily estimated on runtime. This
description was confirmed to accurately describe the mean disturbance of the bound vortex for a large variety of simulations
(Fig. 3).

With our quantitative description of the velocity field near the actuator line, we provide insight into the validity and robust-
ness of any velocity sampling method; a frequently researched topic on which no consensus is reached. The basic assumptions
of velocity sampling methods, generally concerned with averaging (thereby cancelling) or avoiding the disturbance, may be-
come invalid as the vortex changes its size and location depending on simulation settings (represented by Λ). The expected
outcome of any velocity sampling method can be checked with the present description, as is demonstrated in Fig. 6. Moreover,
the present description suggests it may be used to correct for the disturbance, thereby retaining fidelity of the sampled velocity
and avoiding the associated computational penalty. Such a correction would account for biases caused by the bound vortex, but
is insufficient to account for higher frequency velocity fluctuations caused by the ALM.

The present description also provides insight into convergence of simulations. Depending on the velocity sampling method
and Λ, simulations involving actuator lines may become more or less convergent (i.e. sensitive to numerical settings). We argue
that variation due to different outcomes of sampling within the bound vortex is irrelevant for the appropriate representation
of the relevant physical phenomena, thus should not be considered in convergence studies. By splitting the sampled velocity
in "desired" and "disturbance" parts, where the disturbance is a function of the single parameter Λ, we are able to attribute
variation in rotor thrust to sampling velocity within the bound vortex (Fig. 5, appendix B).

Code availability. Options available; work in progress/discuss with editor.

Appendix A: Division between undisturbed/disturbance velocities and their equivalent from simulation data

450   The sampled velocity is a sum of the velocities, composed of: (1) the velocity as it is required by the aerodynamic routine (being based on the principle of mapping lift and drag from "free stream" velocities, as they occur in a wind tunnel or equivalent) and (2) a disturbance, as stated in Eq. (4). The disturbance velocity can be decomposed into multiple contributing disturbances, each related to a different phenomenon, e.g.:

$$\boldsymbol{V}_d = \boldsymbol{V}_{d,\text{bound vortex}} + \boldsymbol{V}_{d,\text{tip vortex}} + \dots = \sum_{i=1}^{N} \boldsymbol{V}_{d,i}$$

455   for any number (N) of phenomena that can be identified to cause deviation from free-stream at the sampling point.

   Subsequently, we can only validate so far as we are able to extract the undisturbed velocity from data. Since we aim to validate only the disturbance of the bound vortex, ideally we extract from data the quantity that represents the undisturbed velocity plus all disturbances *not* of the bound vortex, i.e. in parenthesis:

$$\boldsymbol{V}_s = \left(\boldsymbol{V}_u + \sum_{i=2}^{N} \boldsymbol{V}_{d,i} \right) + \boldsymbol{V}_{d,1}$$

460   where $\boldsymbol{V}_{d,1}$ refers to the disturbance of the bound vortex. Extracting such a quantity is challenging, if not impossible, hence the results (section 3.1) show deviations from our predicted behaviour in regions where we expect other disturbances to become more prevalent (towards the tip). The present method of extracting this quantity is justified by the assumption that for most of the blade, the dominant error is that of the bound vortex.

Appendix B: Convergence and representation of physical phenomena

465   We reiterate the distinction between the convergence of results and the appropriate representation of relevant physical phenomena. Appropriate representation of physical phenomena is that which is sought. It is assumed to be found when convergence occurs. Note the word "relevant" here; a simulation may not appropriately represent the physical phenomena caused by a flapping bird or of the setting sun, but neither are relevant for the problem at hand; including their effects does not change the outcome of the solution.

470   In our analysis of Fig. 5, we argue that when variation in the thrust coefficient C_t is fully explained by variation in Λ, it is explained by the disturbance velocity; another quantity that is a function of only Λ. To understand the extent to which this is true, we consider how C_t changes with Λ, for some small change $\Delta\Lambda$:

$$C_t(\Lambda + \Delta\Lambda) - C_t(\Lambda) = \int_{\Lambda}^{\Lambda+\Delta\Lambda} \left(\frac{\partial C_t}{\partial \Lambda} \right) d\Lambda \tag{B1}$$

We further consider the derivative:

475
$$\frac{\partial C_t}{\partial \Lambda} = \frac{\partial C_t}{\partial \boldsymbol{V}_s} \frac{\partial \boldsymbol{V}_s}{\partial \Lambda} = \frac{\partial C_t}{\partial \boldsymbol{V}_s} \left(\frac{\partial \boldsymbol{V}_u}{\partial \Lambda} + \frac{\partial \boldsymbol{V}_d}{\partial \Lambda} \right) \tag{B2}$$

Since the sampled velocity is the only variable communicated to the wind turbine model, we write C_t as a function of only it, and apply the chain rule accordingly (first equality of Eq. (B2)). Applying Eq. (4) yields the second equality, where we also omit the derivates of $\boldsymbol{V}_s$ to its constituent velocities, since they simply evaluate to unity. We continue the derivation by applying the chain rule to the first term in the parentheses. This is not necessary for the second term, since $\boldsymbol{V}_d$ is a function of
480 Λ only (Eq. (5)).

$$\frac{\partial C_t}{\partial \Lambda} = \frac{\partial C_t}{\partial \boldsymbol{V}_s}_{(1)} \left(\frac{\partial \boldsymbol{V}_u}{\partial \Delta t}_{(2)} \frac{\partial \Delta t}{\partial \Lambda}_{(3)} + \frac{\partial \boldsymbol{V}_u}{\partial \epsilon}_{(4)} \frac{\partial \epsilon}{\partial \Lambda}_{(5)} + \frac{\partial \boldsymbol{V}_d}{\partial \Lambda}_{(6)} \right) \tag{B3}$$

We next consider the relative contribution of each term and how each may be interpreted. We have labelled each component of the equation using a number within parentheses. Derivative (1) is a prefactor that affects all terms equally and does not explain variation with respect to numerical choices. Derivatives (3) and (5) are simple coordinate transforms resulting from the
485 definition of Λ. Derivatives (2) and (4) describe how the undisturbed velocity, i.e. the realisation of flow as it appears within the rotor of the turbine that is inflow to the airfoil and is undisturbed by the airfoil (or blade) itself, varies with respect to numerical choices. Derivative (6) addresses how the disturbance depends on Λ, which is quantified in this work. We repeat here, as we have argued in section 4.2, that the undisturbed velocity determines the representation of the relevant physical phenomena. Its effect on C_t, which we can now pinpoint to derivates (2) and (4) with their respective coordinate transformations (3) and (5),
490 should ideally dominate the behaviour of C_t; in this case the outcome of the simulation changes because a physical variable (i.e. $\boldsymbol{V}_u$) changes, not because of some sensitivity in an erroneous process (i.e. the process that determines $\boldsymbol{V}_d$).

We may now explain the behaviour of Fig. 5. Term (6) indicates that the value of $\boldsymbol{V}_d$ is fully explained by the value of Λ (it is a function of only Λ). This is not true for $\boldsymbol{V}_u$, which, apparent from terms (2) and (4), depends on Δt and ϵ specifically, not on their combined Λ directly. We see a similar explanation of C_t by Λ in the plot (i.e. the collapse to a line or curve), implying
495 that the behaviour of C_t is dominated by some process that directly depends on Λ, i.e. a process as described by term (6). In fact, from Eq. (B3) we can see that if $\boldsymbol{V}_u$ is converged, then contributions to the change in C_t from terms (2) and (4) are zero, and variation in C_t would be fully explained by Λ (and the disturbance velocity). Although the inverse statement (which we pose in the body of this paper, section 4.2) is likely true, it is not certain (i.e. if variation in C_t is fully explained by Λ, we cannot conclude that $\boldsymbol{V}_u$ is converged). This is because derivatives (2) and (4) may possibly describe changes in values of C_t
500 that happen to follow the same curve when plotted against Λ due to their changes in Δt or ϵ, even though their underlying mechanism is completely different. Because we have not quantified exactly how terms (2)+(3) and (4)+(5) behave, we cannot say for certain that it is different from how term (6) behaves. This concludes interpretation of Fig. 5.

Author contributions. EW: Conceptualization, formal analysis, investigation, methodology, software, validation, visualization, writing (original draft preparation); DT: supervision, writing (review and editing); AV: supervision, funding acquisition, writing (review and editing).

505 *Competing interests.* The authors report no competing interests.

Acknowledgements. This research has received funding by the Dutch National Research Council (NWO) under the Talent Programme Vidi scheme (project number 19675).

References

Amiri, M. M., Shadman, M., and Estefen, S. F.: A review of physical and numerical modeling techniques for horizontal-axis wind turbine wakes, https://doi.org/10.1016/j.rser.2024.114279, 2024.

Chetan, M., Yao, S., and Griffith, D. T.: Flutter behavior of highly flexible blades for two- and three-bladed wind turbines, Wind Energy Science, 7, 1731–1751, https://doi.org/10.5194/wes-7-1731-2022, 2022.

Churchfield, M. J., Schreck, S., Martínez-Tossas, L. A., Meneveau, C., and Spalart, P. R.: An advanced actuator line method for wind energy applications and beyond, in: 35th Wind Energy Symposium, 2017, American Institute of Aeronautics and Astronautics Inc, AIAA, ISBN 9781624104565, https://doi.org/10.2514/6.2017-1998, 2017.

Dag, K.: Combined pseudo-spectral / actuator line model for wind turbine applications, Tech. rep., DTU Wind Energy PhD, www.vindenergi.dtu.dk, 2017.

Folkersma, M.: ASPFAST, https://gitlab.com/whiffle-public/aspfast, [Accessed 31-07-2025], 2023.

Forsting, A. R. M., Pirrung, G. R., and Ramos-García, N.: A vortex-based tip/smearing correction for the actuator line, Wind Energy Science, 4, 369–383, https://doi.org/10.5194/wes-4-369-2019, 2019.

Gutknecht, J., Taschner, E., Coquelet, M., Viré, A., and van Wingerden, J. W.: The impact of coherent large-scale vortices generated by helix active wake control on the recovery process of wind turbine wakes, Physics of Fluids, 37, https://doi.org/10.1063/5.0278687, 2025.

Heus, T., Heerwaarden, C. C. V., Jonker, H. J., Siebesma, A. P., Axelsen, S., Dries, K. V. D., Geoffroy, O., Moene, A. F., Pino, D., Roode, S. R. D., and Arellano, J. V. G. D.: Formulation of the Dutch Atmospheric Large-Eddy Simulation (DALES) and overview of its applications, Geoscientific Model Development, 3, 415–444, https://doi.org/10.5194/gmd-3-415-2010, 2010.

Jha, P. K., Churchfield, M. J., Moriarty, P. J., and Schmitz, S.: Guidelines for volume force distributions within actuator line modeling of wind turbines on large-eddy simulation-type grids, Journal of Solar Energy Engineering, Transactions of the ASME, 136, https://doi.org/10.1115/1.4026252, 2014.

Jonkman, B., Platt, A., Mudafort, R. M., Branlard, E., Sprague, M., Ross, H., jjonkman, HaymanConsulting, Slaughter, D., Hall, M., Vijayakumar, G., Buhl, M., Russell9798, Bortolotti, P., reos rcrozier, Ananthan, S., RyanDavies19, S., M., Rood, J., rdamiani, nrmendoza, sinolonghai, pschuenemann, ashesh2512, kshaler, Housner, S., psakievich, Wang, L., Bendl, K., and Carmo, L.: OpenFAST/openfast: v3.5.3, https://doi.org/10.5281/zenodo.10962897, 2024.

Jost, E., Klein, L., Leipprand, H., Lutz, T., and Krämer, E.: Extracting the angle of attack on rotor blades from CFD simulations, Wind Energy, 21, 807–822, https://doi.org/10.1002/we.2196, 2018.

Kleine, V. G., Hanifi, A., and Henningson, D. S.: Non-iterative vortex-based smearing correction for the actuator line method, Journal of Fluid Mechanics, 961, https://doi.org/10.1017/jfm.2023.237, 2023.

Li, Y., Li, L., Ge, M., and Wang, B.: Wake characteristics of a floating wind turbine in yaw under sway motions, Physics of Fluids, 37, https://doi.org/10.1063/5.0293308, 2025.

Liu, L., Franceschini, L., Oliveira, D. F., Galeazzo, F. C., Carmo, B. S., and Stevens, R. J.: Evaluating the accuracy of the actuator line model against blade element momentum theory in uniform inflow, Wind Energy, 25, 1046–1059, https://doi.org/10.1002/we.2714, 2022.

Martinez-Tossas, L. A. and Meneveau, C.: Filtered lifting line theory and application to the actuator line model, Journal of Fluid Mechanics, 863, 269–292, https://doi.org/10.1017/jfm.2018.994, 2019.

Martínez-Tossas, L. A., Churchfield, M. J., and Meneveau, C.: Optimal smoothing length scale for actuator line models of wind turbine blades based on Gaussian body force distribution, Wind Energy, 20, 1083–1096, https://doi.org/10.1002/we.2081, 2017.

545   Melani, P. F., Mohamed, O. S., Cioni, S., Balduzzi, F., and Bianchini, A.: An insight into the capability of the actuator line method to resolve tip vortices, Wind Energy Science, 9, 601–622, https://doi.org/10.5194/wes-9-601-2024, 2024.

Mi, L., Li, B., Chen, H., Zhang, C., Han, Y., and Cai, C. S.: Multiscale coupling wake simulations for a horizontal-axis wind turbine mounted in complex terrains, Energy Sources, Part A: Recovery, Utilization and Environmental Effects, 47, 1817–1835, https://doi.org/10.1080/15567036.2025.2449980, 2025.

550   Mittal, A., Sreenivas, K., Taylor, L. K., and Hereth, L.: Improvements to the actuator line modeling for wind turbines, in: 33rd Wind Energy Symposium, American Institute of Aeronautics and Astronautics Inc., ISBN 9781624103445, https://doi.org/10.2514/6.2015-0216, 2015.

Muscari, C., Schito, P., Viré, A., Zasso, A., and van Wingerden, J. W.: The effective velocity model: An improved approach to velocity sampling in actuator line models, Wind Energy, 27, 447–462, https://doi.org/10.1002/we.2894, 2024.

Rozema, W., Bae, H. J., Moin, P., and Verstappen, R.: Minimum-dissipation models for large-eddy simulation, Physics of Fluids, 27,
555   https://doi.org/10.1063/1.4928700, 2015.

Sanvito, A. G., Firpo, A., Schito, P., Dossena, V., Zasso, A., and Persico, G.: A novel vortex-based velocity sampling method for the actuator-line modeling of floating offshore wind turbines in windmill state, Renewable Energy, 231, https://doi.org/10.1016/j.renene.2024.120927, 2024.

Schalkwijk, J., Griffith, E. J., Post, F. H., and Jonker, H. J. J.: High-performance simulations of turbulent clouds on a desktop PC, Bulletin of
560   the American Meteorological Society, https://doi.org/10.1175/BAMS-D-11-00059.1, 2012.

Schulz, C. W., Netzband, S., Özinan, U., Cheng, P. W., and Abdel-Maksoud, M.: Wind turbine rotors in surge motion: new insights into unsteady aerodynamics of floating offshore wind turbines (FOWTs) from experiments and simulations, Wind Energy Science, 9, 665–695, https://doi.org/10.5194/wes-9-665-2024, 2024.

Shives, M. and Crawford, C.: Mesh and load distribution requirements for actuator line CFD simulations, Wind Energy, 16, 1183–1196,
565   https://doi.org/10.1002/we.1546, 2013.

Soares-Ramos, E. P., de Oliveira-Assis, L., Sarrias-Mena, R., and Fernández-Ramírez, L. M.: Current status and future trends of offshore wind power in Europe, Energy, 202, https://doi.org/10.1016/j.energy.2020.117787, 2020.

Stevens, R. J., Graham, J., and Meneveau, C.: A concurrent precursor inflow method for Large Eddy Simulations and applications to finite length wind farms, Renewable Energy, 68, 46–50, https://doi.org/10.1016/j.renene.2014.01.024, 2014.

570   Sørensen, J. N. and Shen, W. Z.: Numerical modeling of wind turbine wakes, Journal of Fluids Engineering, Transactions of the ASME, 124, 393–399, https://doi.org/10.1115/1.1471361, 2002.

Taschner, E., Folkersma, M., Martínez-Tossas, L. A., Verzijlbergh, R., and van Wingerden, J. W.: A new coupling of a GPU-resident large-eddy simulation code with a multiphysics wind turbine simulation tool, in: Wind Energy, John Wiley and Sons Ltd, ISSN 10991824, https://doi.org/10.1002/we.2844, 2023.

575   Troldborg, N., Sorensen, J. N., and Mikkelsen, R.: Numerical simulations of wake characteristics of a wind turbine in uniform inflow, Wind Energy, 13, 86–99, https://doi.org/10.1002/we.345, 2010.

Zormpa, M., Zilic de Arcos, F., Chen, X., Vogel, C., and Willden, R.: The Effect of Flow Sampling on the Robustness of the Actuator Line Method, Wind Energy, 28, https://doi.org/10.1002/we.2965, 2025.